Cell-Centered Finite-Volume-Based Perfectly Matched Layer for Time-Domain Maxwell System

Krishnaswamy Sankaran, *Student Member, IEEE*, Christophe Fumeaux, *Member, IEEE*, and Rüdiger Vahldieck, *Fellow, IEEE*

***Abstract*—The perfectly matched layer (PML) technique is extended for a cell-centered finite-volume time-domain (FVTD) method. A step-by-step procedure for the performance characterization of the FVTD PML is presented for both structured and unstructured finite-volume meshes. The FVTD PML is compared with the standard first-order Silver–Müller absorbing boundary condition (SM ABC) for practical applications. It is found that the FVTD PML for an unstructured grid achieves a reflection coefficient lower than −40 dB for incident angles up to 45° and outperforms the SM ABC by 15–20 dB.**

***Index Terms*—Absorbing boundary condition (ABC), computational electromagnetics (CEM), finite volume time domain (FVTD), Maxwell's equations, perfectly matched layer (PML).**

I. Introduction

A CELL-CENTERED finite-volume time-domain (FVTD)-based perfectly matched layer (PML) is modeled and characterized in this paper. Ever since its introduction by Bérenger [1], the PML technique has matured and has been applied to a variety of simulation problems mainly in conjunction with the finite-difference time-domain (FDTD) technique [2]–[5]. More recently work is being reported where the PML is also used for other numerical techniques such as the finite-element time-domain (FETD) formulation [6], [7]. In [8], a vertex-centered FVTD model (variational approach) of the PML was reported for scattering problems, but the performance of the PML was not characterized based on its control parameters. This paper extends the PML concept to the cell-centered FVTD approach and systematically characterizes its performance using both structured and unstructured finite-volume meshes. Furthermore, based on reflection-coefficient computation, the suitability of the FVTD PML for practical problems is addressed. The performance of FVTD PML is compared with the standard first-order Silver–Müller absorbing boundary condition (SM ABC). Finally, as a practical example, the reflection coefficient is computed for the truncation of a parallel-plate waveguide using an FVTD PML and is compared with that of the SM ABC.

Manuscript received October 31, 2005. This work was supported by the Swiss Federal Institute of Technology under ETH Research Grant TH-38/04-1.

The authors are with the Laboratory for Electromagnetic Field Theory and Microwave Electronics, Swiss Federal Institute of Technology-ETH Zürich, Zürich CH-8092, Switzerland (e-mail: krishna@ifh.ee.ethz.ch).

Digital Object Identifier 10.1109/TMTT.2006.869704

II. Domain Discretization

A discrete solution to continuum physics requires sampling spatial and temporal quantities into finite space–time cells. Complex curved geometries and the availability of simple, but accurate boundary conditions (BCs) are basic motivations for the development of a co-located finite-volume space–time approach. Each finite-space cell (*control volume*) stores field quantities at the same point in space and time. Solutions at various time stamps are obtained by introducing the flux-conservation principle of the field flow, which forms the basis of the FVTD approach. Particular interest is vested on unstructured control volumes, which correspond, for example, to triangular and tetrahedral meshes in two-dimensional (2-D) and three-dimensional (3-D) models, respectively. For completeness, a brief description of the FVTD method is presented in the following. Readers are referred to [9]–[12] for a detailed explanation on the method.

A. Finite Volume: Definitions

The computational domain $\mathcal{O} \subset \Re^d$ is considered as a union of a finite number of *nonoverlapping conformal* tessellations called cells and are represented as Ω_i; i.e., $\mathcal{O} \ni \Omega_i, \forall i$. We are basically interested in a co-located cell-centered formulation where spatial–temporal variations of field quantities ($\boldsymbol{E}$ and $\boldsymbol{H}$) are stored at each cell center. Strictly speaking, these values are an approximation of the mean field values over the entire cell Ω_i. The field values at different space–time stamps are the solutions to Maxwell's two curl equations written as

$$-\mu\partial_t \boldsymbol{H} = \nabla \times \boldsymbol{E} \tag{1}$$

$$\varepsilon\partial_t \boldsymbol{E} = \nabla \times \boldsymbol{H}. \tag{2}$$

In (1), the electric-current source term inside $\mathcal{O}$ is set to zero. Although the method is applicable to inhomogeneous and anisotropic computational domains, (without loss of generality), a homogeneous and isotropic medium is assumed in this paper. In other words, permeability μ and permittivity ε are constant inside $\mathcal{O}$. Equation (1) and (2) are cast in conservative form with the help of the divergence theorem and integrated over each cell with an appropriate spatial (Ω_i) and temporal (Δt) discretization as

$$\boldsymbol{H}_i^{n+1} = \boldsymbol{H}_i^n - \frac{\Delta t}{\mu V_i}\sum_{k=1}^{f}(\boldsymbol{n}_k \times \boldsymbol{E}_k)S_k \tag{3}$$

$$\boldsymbol{E}_i^{n+1} = \boldsymbol{E}_i^n + \frac{\Delta t}{\varepsilon V_i}\sum_{k=1}^{f}(\boldsymbol{n}_k \times \boldsymbol{H}_k)S_k \tag{4}$$

where each ith cell has a volume V_i and f number of faces. Each kth face has a surface area S_k and an outward normal $\boldsymbol{n}_k$. For spatial discretization, monotonic upstream-centered scheme for conservation laws (MUSCL)-based second-order spatial discretization is used [11], [13]. The formulation used here is completely cell centered as the gradients are computed directly from the neighboring cell center values without any interpolation, as required in [8]. For simplicity, the temporal discretization in (3) and (4) are represented as a first-order Euler discretization. In practice, however, due to stability and accuracy concerns, second-order Lax–Wendroff (predictor–corrector) time stepping is used for temporal discretization. The maximum temporal discretization (Δt) possible for a given mesh geometry is bounded by the *grid speed*—which is the ratio of spatial discretization (linear dimension Δx) to the temporal discretization (Δt). For a structured grid, the term Δt is directly derived using the famous Courant–Friedrich–Lewy (CFL) condition, which satisfies the relation $(\Delta x)/(\Delta t) \leq c$. However, for an unstructured mesh, the value of maximum Δt is bounded by the geometry of the smallest (worst) cell in the entire computational domain. The field values of $\boldsymbol{E}$ and $\boldsymbol{H}$ at time steps "$n+1$" are computed using only their values known at "n," resulting in an explicit FVTD formulation.

III. FVTD-PML Formulation

The cell-centered FVTD formulation of the PML is based on modifying the update equations (3) and (4) with lossy material property in order to absorb the incident electromagnetic (EM) wave as

$$-\mu\partial_t \boldsymbol{H} = \nabla \times \boldsymbol{E} - \sigma^M \boldsymbol{H} \tag{5}$$

$$\varepsilon\partial_t \boldsymbol{E} = \nabla \times \boldsymbol{H} - \sigma^E \boldsymbol{E} \tag{6}$$

where σ^E and σ^M refer to electric and magnetic conductivities, respectively. If a plane wave traveling across a free-space–PML interface satisfies the condition $\sigma^E/\varepsilon = \sigma^M/\mu \equiv \sigma/\varepsilon$ inside the PML domain, then this ensures reflectionless transmission of the plane wave into the PML [1]. For the sake of simplicity and ease of numerical analysis, henceforth a 2-D TE_z model ($\boldsymbol{E}$ field only in the z-direction and the wave propagation is assumed in the xy-plane) is used. The approach presented here can be extended to 3-D without loss of generality. The solutions of the partial differential equations (PDEs) defining the Maxwell system in TE_z form has three unknowns, namely, the transverse electric-field component in the z-direction (E_z) and two magnetic field components in the x- and y-directions, (H_x) and (H_y), respectively. The field vector for this analysis is represented as $\boldsymbol{U} = [H_x, H_y, E_z]^T$, where the superscript T represents the transpose. As proposed in [1], the total electric field E_z is defined as a sum of two unphysical electric field components, namely, E_{zx} and E_{zy} components, i.e., $E_z = E_{zx} + E_{zy}$. The lossy term σ is also correspondingly split into two components denoted as σ_x and σ_y. This leads to the split field equations (including losses) introduced as

$$\mu\partial_t H_x = -\partial_y(E_{zx} + E_{zy}) - (\mu/\varepsilon)\sigma_y H_x \tag{7}$$

$$\mu\partial_t H_y = \partial_x(E_{zx} + E_{zy}) - (\mu/\varepsilon)\sigma_x H_y \tag{8}$$

$$\varepsilon\partial_t E_{zx} = \partial_x H_y - \sigma_x E_{zx} \tag{9}$$

$$\varepsilon\partial_t E_{zy} = -\partial_y H_x - \sigma_y E_{zy}. \tag{10}$$

A. Flux Formulation

The field update equations of the finite-volume formulation are interconnected by the flux function, which facilitates communication between adjacent cells at the respective cell boundaries. The information is transmitted with a finite velocity, which is equal to the velocity of EM waves in the computational medium $\mathcal{O}$. The whole computational domain $\mathcal{O}$ is considered as a union of the main domain $(\mathcal{O}_{\mathrm{main}})$ and the truncated PML domain $(\mathcal{O}_{\mathrm{pml}})$, i.e., $\mathcal{O} \equiv \mathcal{O}_{\mathrm{main}} \cup \mathcal{O}_{\mathrm{pml}}$. For simplicity, free space is assumed for $\mathcal{O}_{\mathrm{main}}$ and a lossy medium with matched impedance in $\mathcal{O}_{\mathrm{pml}}$. The FVTD method demands the preservation of the hyperbolic nature of Maxwell's equation system in order to use the flux splitting technique [11]. To achieve this, the system (7)–(10) is modified using the relation $E_{zx} = E_z - E_{zy}$ [8] as

$$\mu\partial_t H_x = -\partial_y E_z - (\mu/\varepsilon)\sigma_y H_x \tag{11}$$

$$\mu\partial_t H_y = \partial_x E_z - (\mu/\varepsilon)\sigma_x H_y \tag{12}$$

$$\varepsilon\partial_t E_z = \partial_x H_y - \partial_y H_x - \sigma_x E_z - (\sigma_y - \sigma_x)E_{zy} \tag{13}$$

$$\varepsilon\partial_t E_{zy} = -\partial_y H_x - \sigma_y E_{zy}. \tag{14}$$

Integrating the system (11)–(14) over each cell in the computational domain with area A and perimeter S, and employing the divergence theorem results in the following conservative form:

$$\mu\partial_t \int_A H_x\, dA = -\int_S \mathcal{F}_{H_x} \cdot \boldsymbol{n}\, dS - (\mu/\varepsilon)\int_A \sigma_y H_x\, dA \tag{15}$$

$$\mu\partial_t \int_A H_y\, dA = -\int_S \mathcal{F}_{H_y} \cdot \boldsymbol{n}\, dS - (\mu/\varepsilon)\int_A \sigma_x H_y\, dA \tag{16}$$

$$\varepsilon\partial_t \int_A E_z\, dA = -\int_S \mathcal{F}_{E_z} \cdot \boldsymbol{n}\, dS - \int_A \big(\sigma_x E_z - (\sigma_y - \sigma_x)E_{zy}\big) dA \tag{17}$$

$$\varepsilon\partial_t \int_A E_{zy}\, dA = -\int_S \mathcal{F}_{E_{zy}} \cdot \boldsymbol{n}\, dS - \int_A \sigma_y E_{zy}\, dA. \tag{18}$$

The resulting system (15)–(18) still remains nonhyperbolic due to the unphysical nature of field splitting introduced in the PML. Nevertheless, imposing the initial constraint that when $t = 0$, the field $E_{zy} = 0$ inside $\mathcal{O}_{\mathrm{pml}}$ ensures that the resulting system behaves like a hyperbolic system. The term $\mathcal{F} \cdot \boldsymbol{n}$ in (15)–(18) is referred to as the *flux* function in the FVTD formulation. For simplicity, in the following $\mathcal{F}_{(.)} \cdot \boldsymbol{n}$ is denoted as $\zeta_{(.)}$.

Except for the lossy terms (σ_x and σ_y), (15)–(17) refers to the original TE_z formulation of Maxwell's equations. Hence, the standard FVTD formulation is used to update (15)–(17) [11], [14]. However, there is no direct way to compute the flux term in (18). The unphysical field E_{zy} is forced to be zero inside $\mathcal{O}_{\mathrm{main}}$ and it is updated only inside $\mathcal{O}_{\mathrm{pml}}$. In the following, the flux function for (18), i.e., $\zeta_{E_{zy}}$, is modeled using the *Rankine–Hugoniot* jump condition [15].

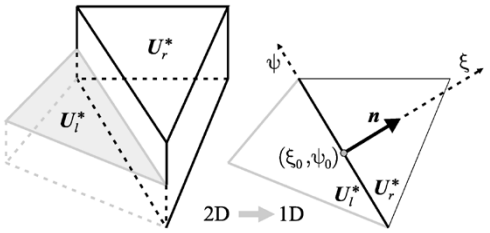

Fig. 1. Split-field flux calculation by 2-D to 1-D transformation (Riemann problem).

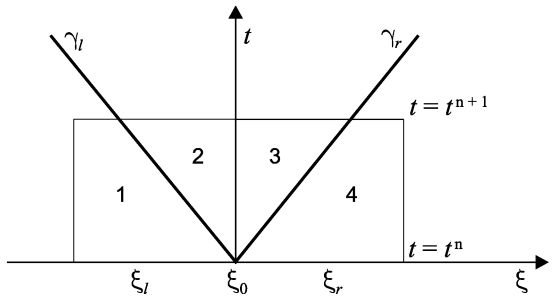

Fig. 2. Solution to 1-D Riemann problem using *Rankine–Hugoniot* jump relation.

B. Split-Field (E_{zy}) Flux Update

The main goal is to update the split-field E_{zy} with a suitable approximation for its flux function $\zeta_{E_{zy}}$. For this, consider any interface between two cells inside the PML domain with some discontinuity, as shown in the 2-D model in Fig. 1. The field values in the adjacent cells, i.e., in the left and right cells, are assumed to be piecewise constant (first-order approximation) and are given by $\boldsymbol{U}_l$ and $\boldsymbol{U}_r$. Due to the discontinuity, the field value at the interface is not readily known. For computing $\zeta_{E_{zy}}$ traversing across the interface, the 2-D problem is transformed into an equivalent one-dimensional (1-D) Riemann problem in the direction normal to the interface, as shown in Fig. 1. The *normalized* normal vector to the interface is written as $\boldsymbol{n} = [n_x, n_y]^T$. The coordinate system of the original problem is transformed to a local coordinate system (ξ, ψ), where ξ and ψ represent the normal and tangential directions to the interface, respectively. The center of the interface is denoted as (ξ_0, ψ_0). It is assumed that the flux variation is only along the normal direction. By transformation to a local coordinate system, it is meant that the system is rotated in the xy-plane by an angle θ. The invariance of Maxwell's system due to rotation helps in applying the same set of equations with an appropriate change of axes ($x \rightarrow \xi$ and $y \rightarrow \psi$). Since there is no variation of field quantities along the tangential direction of the interface, all the gradients along the ψ-direction are reduced to zero. This reduces the 2-D problem into an equivalent 1-D problem with the field variation only along the normal direction of the interface. Since the split-field E_{zy} depends on the field values in (15)–(17), it is sufficient to solve the Riemann problem with the three field values represented by the field vector $\boldsymbol{U}^* = [H_\xi, H_\psi, E_z]$. Hence, the resulting 1-D PDE is written as

$$\partial_t \boldsymbol{U}^* + \partial_\xi \zeta_{\boldsymbol{U}^*} = 0 \tag{19}$$

where ζ represents the flux function. The additional constraints required to solve (19) are given by the initial conditions at time $t = 0$ as

$$\boldsymbol{U}^*(\xi, \psi, t = 0) = \begin{cases} \boldsymbol{U}_l^*, & \xi < \xi_0 \\ \boldsymbol{U}_r^*, & \xi > \xi_0. \end{cases} \tag{20}$$

Considering (11)–(13) and the rotational invariance of the Maxwell system from the global (x, y)-axes to the local (ξ, ψ)-axes, the flux function for (19) is obtained as $\zeta = [0, -E_z, -H_\psi]^T$.

The solution to (19) is uniquely obtained by studying the system-characteristic curves in the space–time plane, as represented in Fig. 2. The characteristics correspond to the direction and speed of propagation of the field solutions at different space–time stamps. In Fig. 2, γ_l and γ_r represents the left and right moving characteristics originating from the interface centre with $\xi = \xi_0$ (compare with Fig. 1). The field values on the left of the interface $(\xi = \xi_l)$ is given by $\boldsymbol{U}_l$ and, likewise, on the right side $(\xi = \xi_r)$ it is equal to $\boldsymbol{U}_r$. The two characteristics (γ_l and γ_r) divide the space–time cell into four distinct regions denoted as regions 1–4 in Fig. 2 with respective field values, namely, $\boldsymbol{U}_1$–$\boldsymbol{U}_4$. In order to solve for the split-field flux $\zeta_{E_{zy}}$, the field values at ξ_0 (see Fig. 2) are required. From (14), the split-field flux function $\zeta_{E_{zy}}$ at the center of the interface (ξ_0, ψ_0) is derived as

$$\zeta_{E_{zy}} = n_y H_{x0} \tag{21}$$

where H_{x0} is the x-component of the magnetic field along the center region with $\xi = \xi_0$. To compute the field values at the center of the interface, the Rankine–Hugoniot jump condition is used. This condition states that the difference in flux across an interface with discontinuity is proportional to the difference in field values across the interface. In the mathematical sense, the above statement reads as

$$\mathcal{A} \cdot (\boldsymbol{U}_2^* - \boldsymbol{U}_1^*) = s_l(\boldsymbol{U}_2^* - \boldsymbol{U}_1^*) \tag{22}$$

$$\mathcal{A} \cdot (\boldsymbol{U}_4^* - \boldsymbol{U}_3^*) = s_r(\boldsymbol{U}_4^* - \boldsymbol{U}_3^*) \tag{23}$$

$$\mathcal{A} \cdot (\boldsymbol{U}_3^* - \boldsymbol{U}_2^*) = s_0(\boldsymbol{U}_3^* - \boldsymbol{U}_2^*) \tag{24}$$

where $\mathcal{A}$ is the Jacobian matrix of the system [11]. The constant of proportionality s_j in (22)–(24) represents the propagation speed of discontinuity due to the jth characteristic. At any time $t > t^n$, s_j is given by

$$s_j = \frac{\xi - \xi_0}{t - t^n}. \tag{25}$$

It is noted that the term $\mathcal{A} \cdot \boldsymbol{U}^*$ numerically corresponds to the flux function $\zeta_{\boldsymbol{U}^*}$. The values of s_j, i.e., the speed at which characteristics propagate, is directly obtained from the eigenvalues of the hyperbolic system. The system considered here has three distinct real eigenvalues. The first eigenvalue is $s_l = -c$ and it moves toward the left side of the interface. The second eigenvalue is $s_r = c$, which moves toward the right side of the interface, and the third eigenvalue is $s_0 = 0$, and is of no numerical importance. It is noted from the value of $\boldsymbol{U}^*$ i.e., E_z, is unaltered by the rotation to local coordinate and, hence, it is required only to find normal and tangential components of the magnetic field

values in regions 2 and 3. Subsequently, using the above discussion and solving (22)–(24) gives unique values of the field in region 2 as

$$H_{\xi 2} = H_{\xi 1} \tag{26}$$

$$H_{\psi 2} = H_{\psi 1} + \frac{1}{2}(c_4\varepsilon_4 E_{z4} - c_1\varepsilon_1 E_{z1}) + \frac{1}{2}(H_{\psi 4} - H_{\psi 1}) \tag{27}$$

where $c_{(.)}$ and $\varepsilon_{(.)}$ correspond to the velocity and permittivity components in the region $(.)$, respectively. Similarly, in region 3, the unique field values are as follows:

$$H_{\xi 3} = H_{\xi 4} \tag{28}$$

$$H_{\psi 3} = H_{\psi 4} + \frac{1}{2}(c_4\varepsilon_4 E_{z4} - c_1\varepsilon_1 E_{z1}) - \frac{1}{2}(H_{\psi 4} - H_{\psi 1}). \tag{29}$$

In order to obtain the field values along the center of the interface, the symmetry of Maxwell's system is used. This approximates the fields at the center region of the interface as an average of the field values from regions 2 and 3 as follows:

$$H_{\xi 0} = (1/2)(H_{\xi 1} + H_{\xi 4}) \tag{30}$$

$$H_{\psi 0} = \frac{1}{2}(H_{\psi 1} + H_{\psi 4}) + \frac{1}{2}(c_4\varepsilon_4 E_{z4} - c_1\varepsilon_1 E_{z1}) \tag{31}$$

where subscript 0 represents the center region. The field values in global coordinates are directly obtained from (30)–(31) by appropriate rotation of matrix $\mathcal{R}$ as follows:

$$\begin{pmatrix} H_{\xi 0} \\ H_{\psi 0} \\ E_z \end{pmatrix} \overset{\mathcal{R}}{\Longrightarrow} \begin{pmatrix} H_{x0} \\ H_{y0} \\ E_z \end{pmatrix}. \tag{32}$$

The rotation matrix $\mathcal{R}$ for a rotation through an angle θ in the xy-plane is written as

$$\begin{pmatrix} \cos\theta & -\sin\theta & 0 \\ \sin\theta & \cos\theta & 0 \\ 0 & 0 & 1 \end{pmatrix} \tag{33}$$

where $\cos\theta = n_x$ and $\sin\theta = n_y$ with the previously defined n_x and n_y (*normalized* normal components of the interface). Using (30)–(31) in (32) gives an expression for H_{x0}. This is the magnetic field that is required to compute the split-field flux $\zeta_{E_{zy}}$ in (21). Hence, the final expression for $\zeta_{E_{zy}}$ is as follows:

$$\zeta_{E_{zy}} = \frac{n_y}{2}(H_{x1} + H_{x4}) - \frac{n_y^2}{2}(c_4\varepsilon_4 E_{z4} - c_1\varepsilon_1 E_{z1}) \tag{34}$$

$$\Rightarrow = \frac{n_y}{2}(H_{xl} + H_{xr}) - \frac{n_y^2}{2}(c_r\varepsilon_r E_{zr} - c_l\varepsilon_l E_{zl}). \tag{35}$$

The final expression of $\zeta_{E_{zy}}$ consists of flux contribution due to upwind flux splitting, which corresponds to the first term on the right-hand side of (35). The second term on the right-hand side in (35) denotes the correction factor generally used in all upwind approximations. Using $\zeta_{E_{zy}}$ along with the other three standard flux terms, the complete system (15)–(18) is updated at different space–time steps with some additional BCs, which are discussed in the following.

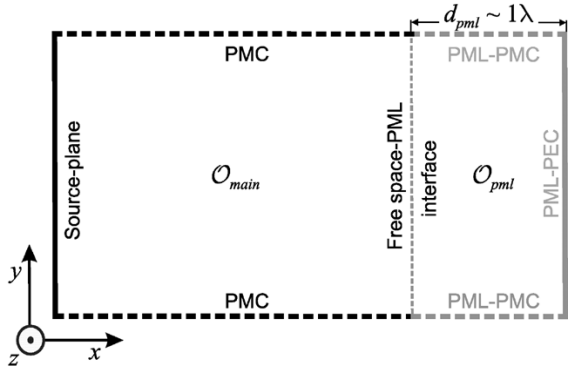

Fig. 3. Model domain used for characterizing FVTD PML.

C. Model Problem—Parallel-Plate Waveguide

The problem used in this paper is a simple parallel-plate waveguiding structure infinitely long in the z-axis, as shown in Fig. 3. A plane wave is simulated by forcing a sinusoidal electric and magnetic field along the boundary plane referred as the *source plane* in Fig. 3. For guiding the plane wave, perfect magnetic conducting (PMC) BC are imposed on both infinite plates inside $\mathcal{O}_{\rm main}$. The computational domain $\mathcal{O}_{\rm main}$ is truncated using a FVTD PML $\mathcal{O}_{\rm pml}$, which extends one wavelength in the (x)-direction (i.e., $d_{\rm pml} = 1\lambda$, unless otherwise stated) and is perpendicular to the x-axis. This thickness is chosen as an empirical tradeoff between computational cost and PML performance. For numerical simplicity and flexibility, the whole computational domain (i.e., both $\mathcal{O}_{\rm main}$ and $\mathcal{O}_{\rm pml}$) is treated as a single entity for the analysis. The split-field (E_{zy}), which plays no role inside $\mathcal{O}_{\rm main}$, is forced to be zero inside $\mathcal{O}_{\rm main}$, and its value becomes important only inside $\mathcal{O}_{\rm pml}$. It is worth noting that the BCs have to be modified in order to take care of the split-field E_{zy} inside $\mathcal{O}_{\rm pml}$, which results in a hybrid PMC BC denoted as the PML PMC. To characterize the FVTD PML, a hybrid perfect electric conducting (PEC) BC (referred as the PML PEC) is used for truncating the FVTD PML. This provides equal reflection of the plane wave for all angles of incidence and, hence, strictly measures the FVTD-PML performance. Furthermore, by using the PML PEC, any additional influence of the truncating BCs (like the SM ABC) on the FVTD PML is also avoided. The split-field flux $\zeta_{E_{zy}}$ for both the PML PMC and PML PEC is computed using only the upwind information without correction factor as

$$\zeta_{E_{zy}} = n_y H_{xl}. \tag{36}$$

The tangential component of electric field (E_z) is zero for the PML–PEC BC. This implies that the correction factor is also zero. For the PML–PMC BC $E_{zl} = E_{zr}$ and, hence, the correction factor becomes zero according to (35). The performance of the cell-centered FVTD PML is analyzed using the above-described model. Various numerical experiments have been carried out and are discussed in depth in Section IV.

IV. Numerical Experiments

Numerical experiments presented in this paper characterize the FVTD PML based on different factors like conductivity profile, PML thickness, convergence, etc. The central idea is to

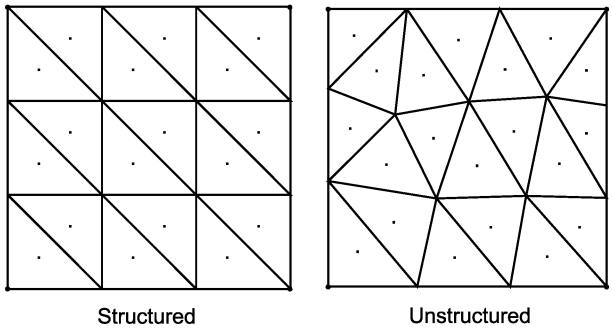

Fig. 4. Structured- and unstructured-type triangular meshes.

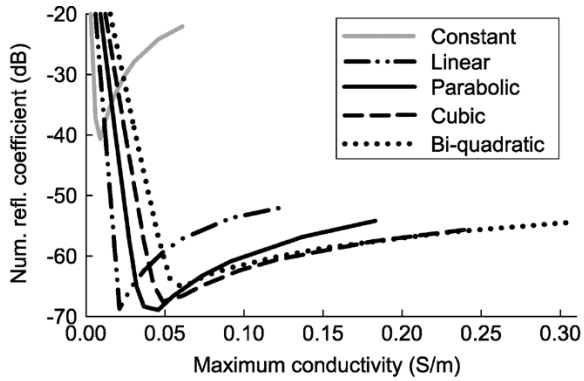

Fig. 5. Numerical reflection coefficient (in decibels) as a function of maximum PML conductivity σ_0 for different profiles.

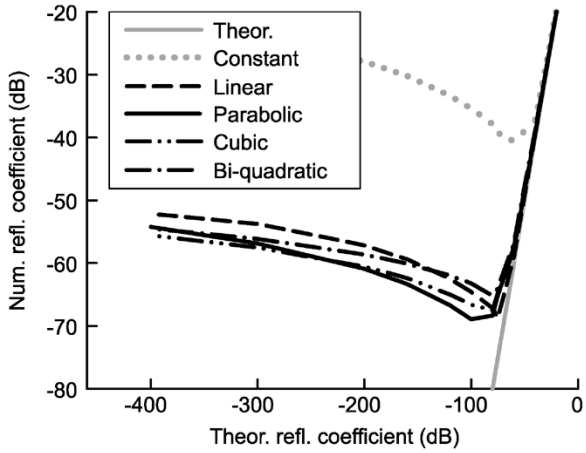

Fig. 6. Numerical reflection coefficient (in decibels) as a function of theoretical reflection coefficient (in decibels) for different profiles.

compare the PML performance using its reflection coefficient (Γ) under different test conditions, i.e., for different thickness, profile, and spatial discretization. To achieve this goal on an unstructured mesh, the whole analysis of the FVTD-PML performance becomes complicated. Hence, the problem is divided into the following two main streams.

1) In the first part of the numerical experiments, an ideally structured FVTD triangular mesh, as shown on left-hand side of Fig. 4, is used in the PML region to investigate the optimal conductivity profile, thickness, and spatial discretization. A structured grid approach is helpful to determine the best possible PML performance that can be achieved using the FVTD method, keeping the mesh-induced errors to the bare minimum.
2) In the second part, knowledge gained from the first set of numerical experiments is applied on a more general setup using a highly unstructured triangular FVTD mesh, as represented on the right-hand side of Fig. 4. Furthermore, to add more practical value to this investigation, the reflection coefficient of the FVTD PML is computed at different angles of plane-wave incidence.

The numerical reflection coefficient (Γ) is computed by subtracting the field values inside the test model from that of a reference. The reference model is built as an extended version of the test model and is truncated at a larger distance from the source.

A. *Influence of the FVTD-PML Profile*

In the discretized PML domain, the variation of the conductivity profile (σ) inside the PML as a function of distance (x) substantially affects its performance. If a constant profile with very high conductivity (σ_0) is used, then the numerical reflection from the free space–PML interface substantially increases. On the other hand, a constant profile with very small σ_0 renders the damping inside the PML ineffective and results in numerical reflections from the truncating boundary (PML PEC). Hence, to study the influence of $\sigma(x)$ and σ_0 on the PML performance, different possibilities for conductivity variations are tested. The variation of $\sigma(x)$ for different profiles is given by

$$\sigma(x) = \sigma_0 \left(\frac{x - x_s}{d_{\mathrm{pml}}} \right)^p \tag{37}$$

where $x = x_s$ is the FVTD PML starting value for the x-coordinate, d_{pml} is the thickness of the PML, and p is the order of profile function. Different values of p, i.e., $p = 0, 1, 2, 3$ or 4, corresponds to five different profile functions, namely, constant, linear, parabolic, cubic, or bi-quadratic profile variations along the x-axis. The results of the profile test as a function of σ_0 are shown in Fig. 5. In principle, a particular value of σ_0 corresponds to a particular value of the maximum expected theoretical reflection coefficient (in decibels) for the FVTD PML. The relation between σ_0 and the theoretical reflection coefficient Γ_{th} is bounded by d_{pml} and the order of conductivity profile p inside $\mathcal{O}_{\mathrm{pml}}$ [1], [16], which is given by

$$\sigma_0 = \left(\frac{\varepsilon_0 c}{d_{\mathrm{pml}}} \right) \left(\frac{p+1}{2} \right) \left(\ln \left(\frac{1}{\Gamma_{\mathrm{th}}} \right) \right) \tag{38}$$

where ε_0 and c represent permittivity of free space and velocity of the EM wave in free space, respectively. The variation of the numerical reflection coefficient as a function of the theoretical reflection coefficient is shown in Fig. 6.

From the results shown in Figs. 5 and 6, it is clearly noticeable that an FVTD PML with a constant profile does not yield satisfactory performance. In spite of the matched impedance condition between the two domains ($\mathcal{O}_{\mathrm{main}}$ and $\mathcal{O}_{\mathrm{pml}}$), high numerical reflection arises from discretization errors in the presence of large conductivity steps. In other words, unlike the continuous case, the discretized field equations are very sensitive to sudden changes in the parameters of adjacent cells. On the

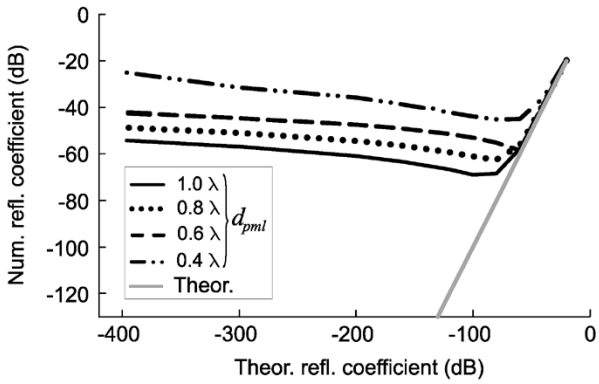

Fig. 7. Numerical reflection coefficient (in decibels) as a function of theoretical reflection coefficient (in decibels) for different FVTD-PML thickness (d_{pml}).

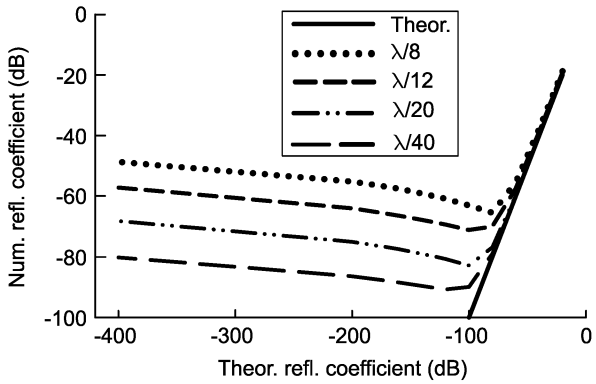

Fig. 8. Numerical reflection coefficient (in decibels) as a function of theoretical reflection coefficient (in decibels) for different spatial discretization.

other hand, a smooth and gradual increase in conductivity allows the impinging EM waves to encounter larger values of $\sigma(x)$ only at some sufficient depth inside the FVTD-PML domain. This helps in attenuating the reflections due to larger values of conductivity deep inside the FVTD PML using the initial damping layers. Among the different options, the parabolic profile allows to reach the lowest reflection coefficient for a given FVTD-PML thickness. Furthermore, the tolerance range of a parabolic profile is larger compared to other options. In the current simulation, with a parabolic profile, it was possible to reach a numerical reflection coefficient (Γ) in the order of -70 dB. Consequently, the parabolic profiling is used for the following further analysis.

B. Influence of FVTD-PML Thickness

Various models for optimal FVTD-PML thickness are simulated in the range $d_{\mathrm{pml}} = 0.4\lambda, \ldots, 1.0\lambda$. The spatial discretization used corresponds to a linear dimension close to $\lambda/10$. The results obtained are shown in Fig. 7. As expected, the performance of the FVTD PML improves as the PML thickness increases. This is mainly due to the increase in damping distance inside the PML. The impinging EM wave undergoes initial damping on the way toward the truncating PML–PEC BC and, after getting reflected from the PML PEC, it is once again damped on the return path toward the free-space–PML interface. The theoretically expected values are also plotted in comparison to the performance of the discrete FVTD-PML model. The results show that a PML thickness of around 1λ is a good choice for most practical problems. This thickness is used for the rest of the numerical experiments.

C. Convergence Analysis of FVTD PML

The discrete model of the PML introduces imperfections in the perfect continuous PML. This imperfection results in a deviation of the discrete solution from the analytical model. Hence, it is instructive to test the rate of convergence for the FVTD-PML model to understand the behavior of the discrete FVTD-PML models for a particular spatial discretization. The results of the convergence test are shown in Fig. 8. For each spatial discretization, the numerical reflection coefficient follows the theoretical counterpart up to a certain value and then starts to deviate. This deviation comes from the roundoff errors in the discrete solutions to continuous problems. The analysis also confirms the convergence of the FVTD-PML model to the analytical solution. A spatial discretization corresponding to a linear dimension of $\lambda/12$ is used in the following investigations of stability and angular wave incidence. This discretization corresponds to common practice in modeling EM problems for practical applications.

D. Broad-Band Characteristics

It has to be pointed out that the performance of the FVTD PML is affected mainly by two frequency-dependent parameters. The first parameter is the thickness of FVTD-PML d_{pml} in terms of λ, which has been investigated in Section IV-B. The second parameter is the spatial discretization in terms of λ, and this has been addressed in Section IV-C. For a pulse excitation, the relevant wavelength corresponds to the lower frequency limit of the incident EM excitation, i.e., $\lambda = \lambda_{\max}$. In principle, for a given spatial discretization, lowering the frequency (e.g., by a factor of 2) increases the wavelength (by a factor of 2), which, in turn, increases the number of points per wavelength. In other words, this makes the spatial discretization finer. Hence, increasing the spatial discretization and decreasing the relative thickness of the FVTD PML have opposite effects. This implies that d_{pml} can be reduced for finer meshes. As a rule-of-thumb, choosing $d_{\mathrm{pml}} = 0.5\lambda_{\max}$ will meet the requirements of most engineering broad-band applications.

E. Stability of FVTD-PML Model

Most of the PML models suffer from stability problems due to an ill-posed discrete model. If the numerical experiment remains stable even for extremely long run-time simulations this then indicates sufficient stability for practical applications. As an experimental approach, the FVTD-PML model is tested for long-time simulation runs (around 2500 time periods). The result of the simulation is shown in Fig. 9. The energy inside the whole computational domain is bounded, and this demonstrates the overall stability of the FVTD-PML model even at very late time steps.

F. Angular Dependence of FVTD-PML Reflection Coefficient

All the aforementioned tests performed at normal incidence provide a guidance in the selection of optimal profile, thickness,

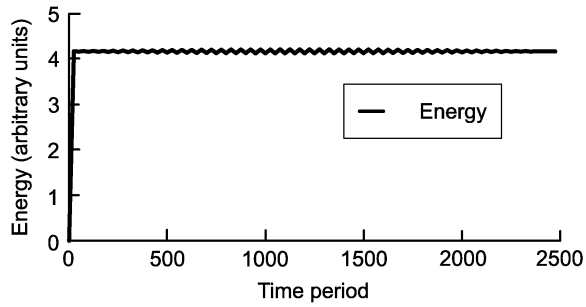

Fig. 9. Energy inside FVTD-PML model as a function of time period.

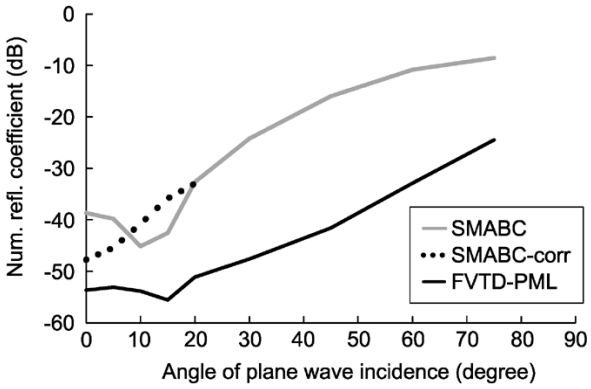

Fig. 10. Comparison of numerical reflection coefficient (in decibels) for different angles of plane-wave incidence for FVTD PML and SM ABC.

and spatial discretization for the FVTD-PML model. However, for use in practical situations, the most relevant characteristic is the performance of the PML in terms of its reflection coefficient at different angles of wave incidence. In addition, a highly unstructured mesh is used to model the angular response in order to represent a more general and practical situation. Furthermore, for the performance comparison, the standard first-order SM ABC is used as a reference BC. The results for the angular wave incidence is shown in Fig. 10.

In theory, the reference SM ABC is accurate for normal incidence. However, in a 2-D simulation, the computation of the gradient suffers from inaccuracies near the domain boundary, as compared to the 3-D case [17]. Hence, there is a slight degradation of performance at normal incidence (0°). Correcting the gradient with an analytical value permits to rectify this numerical degradation, and is shown via dotted lines in Fig. 10. For all angles, the performance of the FVTD PML is 15–20 dB better than the standard SM ABC. It is worth noting that the results presented in Fig. 10 correspond to the worst case scenario. Interestingly, for a variation of incidence angle from 0° to 45°, the performance of the FVTD PML remains better than -40 dB. This result confirms a far better performance than the existing SM ABC and will satisfy the requirements for most practical applications.

G. Practical Application

To demonstrate the application of an FVTD PML for practical problems, a parallel-plate electric waveguide with its two plates separated by a distance of 0.71λ is simulated. A first-order TE mode is forced at the source plane. Both FVTD PML and SM ABC are tested for their numerical reflection coefficients when used as a truncating BC. The spatial discretization used for meshing the waveguide approximately corresponds to a linear dimension of $\lambda/12$. For this setup, the guide wavelength inside the waveguide is approximately 1.4λ, and the angle of incidence at the truncating boundary approximately corresponds to 45°. A numerical reflection coefficient of -16 dB is obtained using an SM ABC. However, when the FVTD PML is employed, the numerical reflection coefficient for the same setup is as low as -42 dB. This clearly proves the excellent performance of the FVTD PML over the SM ABC.

V. Conclusion

The PML technique has been extended to cell-centered FVTD formulation, and a step-by-step characterization procedure has been introduced to study the performance of an FVTD PML based on its control parameters. Various tests have been performed to study the FVTD-PML performance, and an optimal value for its profile and thickness have been numerically derived. Using a structured mesh approach, a numerical reflection coefficient as low as -80 dB has been achieved to demonstrate the maximum achievable limits of the FVTD PML. However, on a more general unstructured grid, the FVTD PML maintains a reflection coefficient lower than -40 dB for incidence angles up to 45°. Hence, for practical applications, the FVTD PML outperforms the existing first-order SM ABC by 15–20 dB.

References

[1] J.-P. Berenger, "A perfectly matched layer for the absorption of electromagnetic waves," *J. Comput. Phys.*, vol. 114, no. 2, pp. 185–200, 1994.

[2] W. C. Chew and W. H. Weedon, "A 3-D perfectly matched medium from modified Maxwell's equations with stretched coordinates," *Microw. Opt.*, vol. 114, no. 2, pp. 185–200, 1994.

[3] S. Gedney, "An anisotropic perfectly matched layer-absorbing medium for the truncation of FDTD lattices," *IEEE Trans. Antennas Propag.*, vol. 44, no. 12, pp. 1630–1639, Dec. 1996.

[4] Z. Wu and J. Fang, "Numerical implementation and performance of perfectly matched layer boundary condition for waveguide structures," *IEEE Trans. Microw. Theory Tech.*, vol. 43, no. 12, pp. 2676–2683, Dec. 1995.

[5] L. Zhao and A. Cangellaris, "GT-PML: Generalized theory of perfectly matched layers and its application to the reflectionless truncation of finite-difference time-domain grids," *IEEE Trans. Microw. Theory Tech.*, vol. 44, no. 12, pp. 2555–2563, Dec. 1996.

[6] Z. Sacks, D. Kingsland, R. Lee, and J.-F. Lee, "A perfectly matched anisotropic absorber for use as an absorbing boundary condition," *IEEE Trans. Antennas Propag.*, vol. 43, no. 12, pp. 1460–1463, Dec. 1995.

[7] T. Rylander and J.-M. Jin, "Perfectly matched layer in three dimensions for the time-domain finite element method applied to radiation problems," *IEEE Trans. Antennas Propag.*, vol. 53, no. 4, pp. 1489–1499, Apr. 2005.

[8] F. Bonnet and F. Poupaud, "Berenger absorbing boundary condition with time finite-volume scheme for triangular meshes," *Appl. Numer. Math.*, vol. 25, no. 4, pp. 333–354, Dec. 1997.

[9] N. K. Madsen and R. W. Ziolkowski, "A three-dimensional modified finite volume technique for Maxwell's equations," *Electromagnetics*, vol. 10, pp. 147–161, 1990.

[10] V. Shankar, A. H. Mohammadian, and W. F. Hall, "A time-domain, finite-volume treatment for the Maxwell equations," *Electromagnetics*, vol. 10, pp. 127–145, 1990.

[11] P. Bonnet, X. Ferrieres, B. Michielsen, P. Klotz, and J. L. Roumiguiéres, *Time Domain Electromagnetics*, S. M. Rao, Ed. New York: Academic, 1997, ch. 9, pp. 307–367.

[12] C. Fumeaux, D. Baumann, P. Leuchtmann, and R. Vahldieck, "A generalized local time-step scheme for efficient FVTD simulations in strongly inhomogeneous meshes," *IEEE Trans. Microw. Theory Tech.*, vol. 52, no. 3, pp. 1067–1076, Mar. 2004.

[13] B. V. Leer, "Toward the ultimate conservative difference scheme (V): A second-order sequel to Godunov's method," *J. Comput. Phys.*, vol. 32, no. 1, pp. 101–136, 1979.
[14] J.-P. Cioni, L. Fezoui, and H. Steve, "A parallel time-domain Maxwell solver using upwind schemes and triangular meshes," *IMPACT Comput. Sci. Eng.*, vol. 5, no. 3, pp. 215–247, 1993.
[15] E. Godlewski and P.-A. Raviart, *Numerical Approximation of Hyperbolic Systems of Conservation Laws*. Berlin, Germany: Springer-Verlag, 1996.
[16] F. Collino and P. B. Monk, "Optimizing the perfectly matched layer," *Comput. Methods Appl. Mech. Eng.*, vol. 164, pp. 157–171, 1998.
[17] D. Baumann, C. Fumeaux, and R. Vahldieck, "Treatment of arbitrary-shaped boundaries with the finite-volume time-domain (FVTD) method," in *17th Int. Electromagn. Compat. Symp./Exhibition*, Warsaw, Poland, Jun. 2004, pp. 445–450.

Krishnaswamy Sankaran (S'98) received the B.Eng. degree (with a first-class distinction) in electrical and electronics engineering from the University of Madras, Madras, India, in 2002, the M.Sc. degree in information and communication engineering from the University of Karlsruhe TH, Karlsruhe, Germany, in 2004, and is currently working toward the Ph.D. degree from the Swiss Federal Institute of Technology (ETH) Zürich, Zürich, Switzerland.

From October 2003 to May 2004, he was a Research Trainee with the European Commission, Joint Research Centre, Ispra, Italy, where he was involved in the field of radar systems engineering and remote sensing. In June 2004, he joined the ETH Zürich, where he is currently with the Laboratory for Electromagnetic Field Theory and Microwave Electronics (IFH). His main research interests are numerical methods for solving EM field problems, computational physics, and applied mathematics.

Mr. Sankaran is the current vice-chair of the IEEE Student Branch Zürich. He was the recipient of a full postgraduate scholarship.

Christophe Fumeaux (M'03) received the Diploma and Ph.D. degrees in physics from the Swiss Federal Institute of Technology (ETH) Zürich, Switzerland, in 1992 and 1997, respectively. His doctoral dissertation concerned antenna-coupled infrared detectors.

From 1998 to 2000, he was a Post-Doctoral Researcher involved in infrared technology with the School of Optics, University of Central Florida, Orlando. In 2000, he joined the Swiss Federal Office of Metrology, Bern, Switzerland, as a Scientific Staff Member. Since 2001, he has been a Research Associate with the Laboratory for Electromagnetic Fields and Microwave Electronics (IFH), ETH Zürich, Switzerland. During Fall 2005, he was a Visiting Scientist with the Laboratory of Sciences and Materials for Electronics, and of automatic (LASMEA), University of Blaise Pascal, Clermont-Ferrand, France. His current main research interest concerns computational electromagnetics in the time domain for numerical analysis of microwave circuits and antennas.

Dr. Fumeaux has been the chairman of the IEEE Swiss Joint Chapter on Microwave Theory and Techniques, Antennas and Propagation, and Electromagnetic Compatibility (EMC) since January 2006. He was the recipient of the ETH Silver Medal of Excellence for his doctoral dissertation. He was the corecipient of the 2004 Applied Computational Electromagnetics Society (ACES) Outstanding Paper Award.

Rüdiger Vahldieck (M'85–SM'86–F'99) received the Dipl.-Ing. and Dr.-Ing. degrees in electrical engineering from the University of Bremen, Bremen, Germany, in 1980 and 1983, respectively.

From 1984 to 1986, he was a Post-Doctoral Fellow with the University of Ottawa, Ottawa, ON, Canada. In 1986, he joined the Department of Electrical and Computer Engineering, University of Victoria, Victoria, BC, Canada, where he became a Full Professor in 1991. During the fall of 1992 and the spring of 1993, he was a Visiting Scientist with the Ferdinand-Braun-Institute für Hochfrequenztechnik, Berlin, Germany. In 1997, he accepted an appointment as a Professor of electromagnetic-field theory with the Swiss Federal Institute of Technology (ETH) Zürich, Zürich, Switzerland, and became Head of the Laboratory for Electromagnetic Fields and Microwave Electronics (IFH) in 2003. His research interests include computational electromagnetics in the general area of electromagnetic compatibility (EMC) and, in particular, for computer-aided design of microwave, millimeter-wave, and opto-electronic integrated circuits. Since 1981, he has authored or coauthored over 300 technical papers in books, journals, and conferences, mainly in the field of microwave computer-aided design.

Prof. Vahldieck is the past president of the IEEE 2000 International Zürich Seminar on Broadband Communications (IZS'2000). Since 2003, he has been president and general chairman of the International Zürich Symposium on Electromagnetic Compatibility. He is a member of the Editorial Board of the IEEE TRANSACTIONS ON MICROWAVE THEORY AND TECHNIQUES. From 2000 to 2003, he was an associate editor for the IEEE MICROWAVE AND WIRELESS COMPONENTS LETTERS, and from July 2003 until the end of 2005, he was the editor-in-chief. Since 1992, he has served on the Technical Program Committee (TPC) of the IEEE Microwave Theory and Techniques Society (IEEE MTT-S) International Microwave Symposium (IMS), the IEEE MTT-S Technical Committee on Microwave Field Theory, and in 1999, on the TPC of the European Microwave Conference. From 1998 to 2003, he was the chapter chairman of the IEEE Swiss Joint Chapter on Microwave Theory and Techniques, Antennas and Propagation, and EMC. Since 2005, he has been president of the Swiss Research Foundation on Mobile Communications. He was the recipient of the J. K. Mitra Award of the Institution of Electronics and Telecommunication Engineers (IETE) (in 1996) for the best research paper in 1995 and was corecipient of the Outstanding Publication Award of the Institution of Electronic and Radio Engineers in 1983. He was the corecipient of the 2004 Applied Computational Electromagnetic Society (ACES) Outstanding Paper Award.